

Broadband visco-acoustic Q factor imaging by seismic tomography and instantaneous frequency

R. Lin¹, A. Vesnaver¹, G. Böhm² and J. M. Carcione²

¹ *Khalifa University of Science and Technology – Petroleum Institute, Petroleum Geoscience Department, P.O. Box 2533, Abu Dhabi (United Arab Emirates). E-mails: avesnaver@pi.ac.ae , linrongzhi89@qq.com*

² *OGS – Italian National Institute for Oceanography and Applied Geophysics, Borgo Grotta Gigante 42/c, 34010 Trieste (Italy). E-mails: gbohm@inogs.it , jcarcione@inogs.it*

SUMMARY

Recent advances in seismic acquisition and processing allowed enhancing significantly the imaging resolution, mainly by broadening the signal bandwidth towards the lower frequencies. So far, however, frequencies lower than a few Hz cannot be obtained by standard surveys, and this gap is normally filled by estimating those components using velocity analysis. In this paper we propose a similar approach for imaging the anelastic absorption, i.e., by merging a low-frequency component given by reflection tomography with the high-frequency component derived from the instantaneous frequency. First, a macro-model in depth is built by traveltimes and Q-factor tomography; then, this model is combined with the high-frequency component obtained from the depth migrated instantaneous frequency. We get so a broadband Earth model for the Q factor, using a consistent velocity field provided by the traveltimes inversion of direct and reflected arrivals. This new hybrid method is applied to a 2D synthetic example.

Key words: Seismic attenuation; Seismic tomography; Joint inversion; Image processing; Numerical modelling.

1 INTRODUCTION

Anelastic absorption is a key factor that limits the resolution of seismic imaging, but provides clues about the presence of fractures and saturating fluids in hydrocarbon reservoirs. Unfortunately, different concurring phenomena reduce the high-frequency content in the seismic signals, as multiple scattering and thin layers, beside the intrinsic absorption due to the rock matrix and filling fluids (Futterman 1962; White 1966; Spencer *et al.* 1982; Wu 1985; Nur 1989; Carcione 2014). As a result, an averaged anelastic absorption is actually estimated by methods as the spectral ratio or the frequency shift (Quan & Harris 1997; Rossi *et al.* 2007, 2011). Efforts are ongoing for decomposing such a cumulative effect into a scattering contribution and a petrophysical component, consistent with core analysis, well logs and VSPs (see Kjartansson 1979; Raikes & White 1984; Jannsen *et al.* 1985; Tonn 1991; Zucca *et al.* 1994; Dasgupta & Clark 1998; Hackert & Parra 2003 2004; Cheng & Margrave 2012; Dupuy *et al.* 2016 a, b; Amoroso *et al.* 2017, among many others). This paper aims at reducing the ambiguity of this decomposition by a new hybrid approach, combining tomography and migration for estimating the velocity and imaging the Q factor in sequence, linked by a shared Earth model in depth.

Another major ambiguity is the cross-talk between local anomalies in the P velocity and Q factor. Ribodetti & Virieux (1998) developed a method for inverting SH waves for visco-acoustic parameters, based on a Born approximation. However, SH waves are rarely recorded properly in standard surveys for oil and gas exploration and production. When studying more general wave types, Mulder & Hak (2009a, b) showed that almost identical seismic responses are obtained from different visco-acoustic Earth models, if their complex velocities are weighted Hilbert transforms of a reference model. This ambiguity may be reduced by imposing causality conditions in the imaging, but at the cost of a slow convergence in an iterative process (Hak & Mulder, 2011). Such a result discourages attempts for a joint inversion of velocities and Q factor, unless other data or constraints are available, as calibrations by well logs or vertical seismic profiles. Our approach partially overcomes

such a major drawback, as velocities are estimated first, kept fixed and used later for the Q factor estimation. We show that a key contribution to get high-resolution images of the Q factor comes from the depth migration of the instantaneous frequency.

2 MACRO-MODEL

Traveltime inversion is a reliable tool for building a 3D macro-model in depth for the P and S velocity, especially when reflected, refracted and diving waves are jointly inverted, ideally merging surface and borehole data (Vesnaver *et al.* 2000; Rossi & Vesnaver 2001; Rossi *et al.* 2001; among others). This acoustic or elastic Earth model is a low-resolution starting point for a more detailed image, obtained by pre-stack depth migration using the velocity estimated by the full-waveform inversion (Tarantola 1984; Mora 1989; Operto *et al.* 2004; Plessix 2008; among others). Such an image is an estimate of the reflectivity, which depends on the acoustic impedance contrast.

A resolution increase of the velocity field may be obtained by picking and inverting not only major continuous reflected arrivals, but also sparse coherent events (Sword 1986; Billette & Lambaré 1998). Various semi-automatic methods were proposed for these events recognition (Guillaume *et al.* 2001; Billette *et al.* 2003; Fei & McMechan 2006) that got encouraging results, but still require a careful tuning of processing parameters and quality control of the result. In this paper, we aim at increasing the Earth model resolution by linking a macro-model obtained by tomographic inversion over a few reflectors with a micro-model obtained by imaging. The latter one does not require an interpretative processing, so moving closer to a data-driven procedure.

The same picked traveltimes for estimating the P (or S) velocity field and interfaces' structure are used for windowing the seismic wavelets of the main reflections, to estimate the Q factor too. The centroid of their spectrum is compared with that one assumed for the seismic source, or with a chosen reference signal, as a shallower reflection. We estimate the contrast in anelastic absorption by solving the following equation (Quan & Harris 1997):

$$\int_{ray} \alpha(\mathbf{x}) d\mathbf{l} = (C_s - C_w) / \sigma_s^2 = F \Phi_{sw} \quad (1)$$

where σ_s^2 is the spectral variance of the source pulse, F is its inverse, and Φ_{sw} is the centroid shift due to the anelastic absorption. Equation (1) relates the source spectrum centroid C_s and that of the picked wavelet C_w (at the receiver) to the integral along the ray path of the absorption coefficient $\alpha(\mathbf{x})$, expressed in m^{-1} . The absorption is a function of the 3D vector coordinates \mathbf{x} . The ray path is available from the traveltimes inversion, together with the velocity field. The factor F in (1) depends on the source spectrum, which can be assumed to be known and constant within a normal seismic survey. This assumption is realistic for marine surveys, while it may be weak for land surveys with a complex near surface. The variations of source and receiver coupling can be compensated, in principle, by a surface-consistent deconvolution (Taner & Koehler 1981). With this *caveat*, each picked signal provides an equation as (1), which can be discretized for each ray i and solved for the values α_j as a linear equation system:

$$\sum_j \alpha_j l_{ij} = \Phi_i / \sigma_s^2 \quad , \quad (2)$$

where α_j is the absorption coefficient in the pixel j , and the coefficients l_{ij} are the path length of ray i in the pixel j , i.e., the same as for the traveltimes inversion (Rossi *et al.* 2007, 2011). The same picked signals are used first for inverting their traveltimes for P velocity, and later for windowing their wavelets and getting their centroid spectrum for the Q factor estimation by (2). Both P velocity and Q factor are constant within each pixel, but they can change in the 3D Earth model arbitrarily.

The Q factor $Q(\mathbf{x})$ depends both on the anelastic absorption coefficient $\alpha(\mathbf{x})$ and the local velocity $v(\mathbf{x})$:

$$Q(\mathbf{x}) = \pi f / [v(\mathbf{x}) \alpha(\mathbf{x})] \quad . \quad (3)$$

where f is the frequency (Carcione 2014; eq. 3.129). This relationship may be simplified in the limited bandwidth of seismic surveys by introducing a kind of average attenuation coefficient $\alpha_0 \approx \alpha / f$, getting the following equations (Quan & Harris 1997):

$$Q_j = \pi / [v_j \alpha_{0j}] \quad . \quad (4)$$

where v_j and Q_j are, respectively, the P velocity and Q factor estimated in the pixel j . As we use the same model discretization for P velocity and Q factor, they are computed consistently.

The inversion of picked traveltimes and wavelets for the most prominent signals provides a visco-elastic macro-model for the Earth in depth, which can be used directly for the pre-stack depth migration. Another use is the initial model for full-waveform inversion, which is quite dependant on its proximity to the true solution. By improving the initial model, the convergence becomes normally faster and more reliable.

3 MICRO-MODEL

The instantaneous frequency is the time-derivative of the instantaneous phase and may provide an estimate of the Q factor variations in the time domain. Ackroyd (1970) proved that the instantaneous frequency is the centroid of the instantaneous spectrum of a signal. Saha (1987) pointed out that this relationship is exact only at the maxima of the signal envelope, while otherwise is only an approximation. Despite these well-known relationships, this property of the instantaneous frequency has not been fully exploited because of the available algorithms to compute it, requiring the phase unwrapping. Recently, Poggiagliolmi & Vesnaver (2014) proposed a new method based on derivatives and Hilbert transform, which is quite robust and stable. Their algorithm is based on the normalized complex trace $n(t)$ associated to a real trace $r(t)$, using the following relations:

$$c(t) = r(t) + i \text{Hilb}\{r(t)\} \quad , \quad n(t) = c(t) / |c(t)| \quad , \quad (5)$$

where $\text{Hilb}\{\cdot\}$ indicates a Hilbert transform, $c(t)$ is the usual complex trace and its module $|c(t)|$ is the envelope (Taner *et al.* 1979). The instantaneous frequency $\phi'(t)$ is obtained by this formula:

$$\phi'(t) = -i n^*(t) n'(t) \quad , \quad (6)$$

where the primes indicate a time derivative and the asterisk a complex conjugate. The instantaneous phase $\phi(t)$ can be obtained by the time integration of (6), without any cumbersome unwrapping procedure. Additional details, software code and examples are provided by Vesnaver (2017).

If we take a moving average or median filtering over a time window with the duration of a wavelet, the instantaneous frequency can provide a continuous estimate of the spectrum centroid $cw(t)$ as a function of time, within the frequency range of the seismic signal. To link this detailed information to the macro-model in depth obtained by tomography, we have to allow for the 3D distribution of scattering bodies and interfaces. Indeed, the frequency shift method estimates the anelastic absorption along a given ray path, which is found by a coupled traveltimes inversion (Quan & Harris 1997, Rossi *et al.* 2007, 2011). The back-propagation of the absorption anomalies is carried out by the tomographic inversion for a few picked signals, along the related raypaths. When it comes to entire seismic traces, this back-propagation is performed by migration.

A straightforward solution for moving directly from time to depth domain may be a pre-stack depth migration, because traveltimes inversion provides a good macro-model for velocities in depth. From a kinematic point of view, we may expect a correct relocation of scattering bodies and interfaces in their correct position and shape. However, the instantaneous frequency does not conform to the wave equation, and thus the dynamic part may be inaccurate. Other methods have been presented to estimate the anelastic absorption complying with the wave equation, but applicable to special cases (Ribodetti & Virieux 1998) or adopting different algorithms (Hak & Mulder 2011). A viable solution is to carry out a pre-stack time migration to compensate for diffractions and improving the signal/noise ratio, first. A zero-offset time section may be so obtained, which can be used for computing the instantaneous frequency by (6). For complex structures with severe dips, a ray-theoretical migration may be needed (Larner *et al.* 1981), while for gentle dips a plain vertical stretching using the tomographic velocities will convert the migrated $cw(t)$ into the depth-converted centroid $cd(\mathbf{x})$ as a function of the model coordinates \mathbf{x} .

From the difference between the source and the signal spectrum centroid, we get a frequency shift function in depth:

$$\Phi(\mathbf{x}) = C_s - M[cw(t)] = C_s - cd(\mathbf{x}) \quad , \quad (7)$$

where $M[\cdot]$ indicates a migration operator, which remaps the centroids from the time domain to the actual location of the scattering points that produced the analysed waveform. C_s is a constant for a given source type, when assuming an isotropic radiation pattern. When major deviations are expected from this assumption, the data may be pre-conditioned by a surface-consistent deconvolution, which can reduce the offset dependency of the waveforms as well as local coupling variations of sources and receivers.

To be physically consistent, the frequency shift function must be always positive for primary reflections, as the centroid of the recorded signal must be equal or smaller than that of the source. Equation (6) provides a smooth function for the instantaneous frequency, unless data are contaminated by random noise or multiples. In that case, spikes and negative frequencies show up, and a median filter is an effective tool for removing them (Vesnaver 2017).

To estimate the Q factor variations in space from the centroid shift, we can exploit equation (1), as it links this shift to the integral of the absorption coefficient α along a ray. If we may approximate the ray paths of the zero-offset depth migrated section of $\Phi(\mathbf{x})$ by vertical lines, equation (1) simplifies to:

$$2 \int_0^z \alpha(x) dz = F \Phi(\mathbf{x}) \quad (8)$$

where the factor 2 on the left allows for the two-way propagation path of reflected arrivals. Taking the partial derivatives on both sides with respect to z and rearranging, we get:

$$\alpha(\mathbf{x}) = \frac{F}{2} \frac{\partial \Phi(\mathbf{x})}{\partial z} \quad (9)$$

The $\alpha(\mathbf{x})$ value so obtained provides the Q factor using the equation (3). In the more general case when ray bending is not negligible, a gradient operator must be used instead along image-ray trajectories (Hubral & Krey 1980; Larner *et al.* 1981). This happens when relevant velocity changes occur along dipping interfaces.

Any conversion from time to depth domain introduces a locally-varying stretching of the original waveforms, because velocities change in the 3D Earth model. Stretching does not change the relative amplitudes of signals, but certainly their frequency content. Thus, when velocities change significantly within the investigated area, e.g., in presence of salt domes, equation (9) should be modified to allow for this effect.

The workflow for estimating the micro-model can be summarized as follows:

- Estimate a spectrum centroid in the time domain by the instantaneous frequency.
- Convert this estimate into the depth domain by using the velocity macro-model provided by traveltime tomography.
- Compute the coefficient absorption $\alpha(\mathbf{x})$ according to equations (8) and (9).
- Obtain the Q factor $Q(\mathbf{x})$ from equation (3), still using the velocity macro-model from tomography.

4 LINKING MICRO- AND MACRO MODEL

When measuring the same signal in two different frequency bands, recombining them into a consistent broadband signal is not just a plain summation. This case applies only when the acquisition and processing systems for the two bands have identical flat amplitude floors. In the sketched plot in Figure 1 (top), the impulse response of the recording and processing systems are approximated by an Ormsby filter with corner frequencies (A_i, B_i, C_i, D_i) - (see Yilmaz 2001; among many others). Even in these ideal measurement conditions, the possible overlapping part (Figure 1, bottom, in green) must be subtracted. In general, the acquisition sensitivity in the two bands is different, so at least a scaling factor must be introduced to compensate for such a difference. If there is not overlap (Figure 1, top), the total spectrum becomes a linear combination of the two composing bands:

$$\text{Total spectrum} = \lambda_1 \text{ Spectrum } (A_1, B_1, C_1, D_1) + \lambda_2 \text{ Spectrum } (A_2, B_2, C_2, D_2) \quad . \quad (10)$$

The coefficients λ_1 and λ_2 should be estimated to balance the system response in the two bands, so preserving their relative amplitude in the total spectrum. In case of a possible overlapping band (Figure 1, bottom), the spectra scaling should be preceded by the subtraction of the redundant part:

$$\begin{aligned} \text{Total spectrum} = & \lambda_1 \text{ Spectrum } (A_1, B_1, C_1, D_1) + \\ & + \lambda_2 \left[\text{Spectrum } (A_2, B_2, C_2, D_2) - \text{Spectrum } (A_2, B_2, I_{12}, D_1) \right] \end{aligned} \quad (11)$$

We may use the overlapping part to compute an optimal ratio between λ_1 and λ_2 , by imposing the average amplitude to be the same for the two bands. This condition would provide their mutual ratio, but not the absolute value of λ_1 and λ_2 : if so, we would estimate only relative variations. However, if one or more calibration profiles are available, as well logs or VSPs, we can get an absolute Q factor estimation in both bands. Without calibration wells or overlapping frequency bands, the combination of the two components could be only qualitative, ideally based on geological models or geostatistical relationships.

5 APPLICATION EXAMPLE

Figure 2 shows a 2D synthetic model, composed of homogeneous layers with gently bent interfaces. The blue arrows indicate three major discontinuities in terms of P velocity and Q factor that, in geological terms, they mimic the top of the cap rock, and the top and bottom of the reservoir. They identify our macro-model, i.e., a coarse one composed of 3 layers over a half space. The complete model is actually obtained by splitting those thick layers (or macro-layers) into a few thinner micro-layers, with minor perturbations of the macro-model parameters, for a total of 15 items. Note that the colour scale is chosen just to distinguish the different layers. The values of P velocity, Q factor and density are reported in Table 1 for all layers in the model.

We computed synthetic seismograms by discretizing the detailed model by a grid with 1365 x 1326 points, spaced 10 m apart in the horizontal and 5 m in the vertical direction. The simulation was

carried out by running a visco-acoustic pseudo-spectral code (Carcione, 1992; Casula and Carcione, 1992). The algorithm is based on one standard-linear solid (or Zener) element, whose relaxation peak (maximum attenuation) is assumed to be located at the central frequency of the source. An absorbing boundary area, 35 grid points wide, has been introduced to avoid wraparound at the model boundaries (Kosloff & Kosloff 1986), so leaving as the effective model part that one delimited by the black rectangle in the figure. The dotted lines indicate where sources and receivers are placed, that is, at the datum plane of the survey, at a depth of 140 grid points in the modelling mesh. The receivers (1295) are located at each grid point, except in the absorbing boundaries, and the sources (129) are placed every 10 receivers. Thus, the interval among receivers is 10 m, and among sources is 100 m. The source signal is a Ricker wavelet with a dominant frequency of 30 Hz, the sampling rate is 1 ms, with a total record length of 5 s.

Figure 3 displays the P velocity and Q factor for the effective part of the model: only a few of the thin layers can be distinguished visually. They are composed of homogeneous layers with interfaces defined by cubic splines. A minimum-time ray tracing method is adopted to defined the ray paths, for both velocity and Q factor estimation (for further details, see Vesnaver 1996). They are the ideal inversion result if our acquisition and processing system had an infinite frequency band. In reality, surface seismic surveys for oil and gas exploration have a frequency band comprised between 4 and 100 Hz. Seismic tomography can provide macro-models that fill most of the gap up to the zero-frequency limit. Figures 4 and 5 show the low- and high-pass filtered images of the models in Figure 3 using a spatial frequency threshold of 3 m^{-1} in the vertical direction, which approximate what we may expect from the macro- and micro-model estimation. A simple but remarkable argument in these figures is that the high-pass models include both positive and negative values, which may seem un-physical for positive defined quantities as velocity and Q factor. However, this is due to our data processing only. We can expect oscillations across the zero, when our data does not include information about the continuous component.

Comparing the low-pass filtered models for both velocity and Q factors in the Figures 4 and 5, we can notice only minor differences. The information about the fine layers composing the model is mainly provided by the high-frequency component (Figure 5), while the main discontinuities corresponding to the macro-layers show up in the low-frequency component (Figure 4). For this reason, inverting only the horizons corresponding to the interfaces of the macro-model may provide a good approximation of the low-frequency component of the actual model. Thus, picking only those horizons is a practical, cost-effective solution to mitigate the main drawback of P velocity and Q-factor tomography, i.e., the cumbersome pre-stack event interpretation and picking.

The plain summation of corresponding items in Figures 4 and 5 would reproduce the full-spectrum models in Figure 3. All figures are normalized by their maximum value. In these models, the contrast in the Q factor images (at right in Figures 3 to 5) is higher than for the P velocity (at left). Indeed, the Q factor ranges from 50 to 250, so with a ratio 5 between minimum and maximum, while P velocities range from 1474 to 3536 m/s, so with a ratio 2.4 only. Of course, these ratios may be even reversed in other models, but in general we may expect a comparable image quality, in terms of contrast, from either one of these two parameters' inversion.

Figure 6 and 7 show the sections of a synthetic shot gather from the model in Figure 2 and the corresponding instantaneous frequency, computed using the method of Poggiagliolmi & Vesnaver (2014). The differences between the two plots are quite visible: the instantaneous frequency is mainly positive (black colour) and composed of lower frequencies. While the kinematic of the reflections is the same in the two sections, their relative amplitude is similar, but not identical. Indeed, minor differences may be expected, as seen when comparing the high-pass filtered Earth models in Figures 4 and 5 for both P velocity and Q factor. As the density is almost constant, we may assume that the acoustic impedance variations causing the reflectivity is mainly due to the velocity contrast. Within such a crude approximation, we may look at the seismic traces as an image of the velocity model variations, and the instantaneous frequency as an attribute related to the Q factor model variations.

The seismic signal and its instantaneous frequency image the same object boundaries and span a frequency range that is different. Figure 8 shows the average amplitude spectrum of the gathers in Figures 6 and 7. The shot gather spectrum (blue line) exhibits the main peak at about 20 Hz. This value is lower than 30 Hz, i.e., the dominant frequency of the Ricker wavelet we used to model the source in the visco-acoustic simulation, because it includes later events with a dominant frequency decreased by the propagation effects. The instantaneous frequency spectrum (orange line) is shifted towards much lower frequencies, mainly in an interval from 0 to 20 Hz, and this is consistent with the much broader waveforms in Figure 7, when compared to those in Figure 6.

A mild basic processing was applied to the seismic traces, avoiding to distort the frequency changes of direct and reflected signals due to the propagation through a visco-acoustic medium. We compensated the spherical divergence effect using stacking velocities, and removed a few traces acquired close to the absorbing boundary areas at the model sides. The traveltimes of the direct arrivals and the three main reflections were picked to build a macro-model for both P velocity and Q factor, which approximate the corresponding true models quite well (Figure 9). The inversion algorithm is based on staggered grids (Vesnaver & Böhm 2000) and the simultaneous inversion reconstruction technique (SIRT) (see e.g. van der Sluis & van der Vorst 1987; among others). In each layer, a grid of 20 cells was staggered horizontally 4 times, so ending up to a nominal lateral resolution of 80 cells, corresponding to a space interval of 175 m. However, because of the low-pass filtering effect of the staggered grid method, the actual obtained resolution is normally lower. A quantitative comparison about actual and estimated velocity and Q factor can be found in Table 2. We considered a few depth reference levels and averaged the P velocity and Q factor along them, both for the actual models and the estimated ones. The errors are a few percentage points only in all cases.

We notice in Figure 9 that the estimate velocity is very smooth along the layers (upper plot), while a few vertical bars show up for the Q factor (lower plot). The lateral stability may be improved by modelling or acquiring longer offsets, getting diving or head waves to be jointly inverted with the

direct and reflected arrivals (see, e.g., Vesnaver *et al.*, 1999, Rossi *et al.*, 2000). However, we may expect a lower stability for the Q factor in any case, because it is computed by the inverse product of velocity and anelastic absorption (equation 4): thus, errors in these two factors accumulate in the Q estimation.

After the macro-model for P velocity and Q factor has been estimated by tomography, the next step is increasing the resolution by getting the corresponding micro-models. The P velocity field obtained from tomography was used for the pre-stack depth migration of both seismic traces (Figure 10, top) and their instantaneous frequency, followed by a derivative with respect to the depth (bottom). The two sections look very similar in terms of reconstructed structures, but quite different in terms of frequency content, as expected from the spectra comparison in Figure 8. Taking the derivative of the instantaneous frequency with respect to z , we get an estimate for the high-frequency component of the anelastic absorption coefficient (Figure 10, bottom), using equations (4) and (9). The result looks satisfying from a kinematic point of view also at the flanks of the anticline, where the assumption a nearly vertical ray path is violated.

When adopting the other imaging strategy, reversing the order of the operators: migration first, followed by the calculation of the instantaneous frequency. Theoretically speaking, such an order is more rigorous, because the time-domain seismic traces may be migrated using the wave equation, while a seismic attribute as the instantaneous frequency is not supposed to do so. Thus, we may expect that the migrated signal amplitudes are not perfect; on the other hand, the kinematics is the same in both cases, and so the structural reconstruction should not suffer too much. We notice that this more rigorous second approach get worse results. Figure 11 shows the instantaneous frequency computed after the pre-stack time migration (top), and its depth conversion by a vertical stretch using the P velocity model in Figure 9, followed by a derivative along the vertical axis (bottom). We notice numerical dispersion effects both at the anticline flanks and at the image borders. Also, the structure of the “reservoir base” is less accurate, at a depth between 3 and 3.5 km. Thus, the direct

pre-stack depth migration of the instantaneous frequency seems a more effective approach in this case.

The next step is the combination of micro- and macro model to get a broadband image of the Q factor. Figure 12 shows, from left to right, the amplitude spectra of the estimated micro- and macro-model for the anelastic absorption, their linear combination using scaling factors computed as detailed in the Appendix, and the spectrum of the true Earth model. We see that the spectrum obtained combining the high- and low-frequency components resembles that one of the true Earth model better than what each component is achieving separately. At the borders, all information is provided by tomography, because the pre-stack depth migration is fading out there.

The linear combination of the micro- and macro-model provides us with a broadband model for the anelastic absorption $\alpha(\mathbf{x})$. By introducing it in the equation (4), we get the final Q factor estimate displayed in Figure 13. Both the main macro-layers and their finer composing layers are clearly visible. The deepest interfaces are affected by the typical vertical stretching of waveforms produced by the depth migration, due to the higher velocities in the deeper layers. We notice also that some interface are quite faint in the overburden, and better visible in the reservoir layers. In the latter ones, indeed, the Q-factor contrast is larger than elsewhere. This fact highlights that the reflection strength of conventional traces, due to acoustic impedance contrasts, is independent from that one due to Q-factor contrasts (Lines *et al.* 2008, 2011), which we obtained by the instantaneous frequency.

This result shows that we can estimate first the low-frequency components by a tomographic macro-model, where only a few major interfaces are interpreted and their reflected arrivals are picked and inverted, for both P velocity and Q factor. The velocity macro-model can be used for the pre-stack depth migration of the instantaneous frequency, which provides the high-frequency component of the anelastic absorption coefficient, and ultimately the Q factor. The obtained information can be used by interpreters immediately, as information for the reservoir characterization; in addition, it can be an accurate initial model for a visco-acoustic full-waveform inversion.

6 DISCUSSION

The proposed method is expected to mitigate the mix of intrinsic attenuation, due to energy absorption, and the apparent one, due to diffractions and random scattering. This second component is reduced by both pre-stack migration and reflection tomography, which penalize the events that do not fit the velocity field of primary reflections. However, we cannot claim that these contributions are singled out: further developments are still needed to this goal.

A few aspects of the proposed method require further tests. One of those is the robustness of Q estimates with respect to the noise. Poggiagliolmi & Vesnaver (2014) and Vesnaver (2017) showed by synthetic examples that the instantaneous frequency computed by equation (6) is more stable than other methods requiring the instantaneous phase unwrapping. In addition, a median filter with a length comparable to the signal duration (or wavelet) can reduce the distortions up to a signal/noise ratio limit of 100 to 1. Finally, random noise may be smeared out when carrying out the pre-stack time or depth migration but, if its level is quite low, mostly it is reduced further.

Robustness with respect to noise and even null-space related ambiguities is a built-in feature of the staggered grid inversion we adopted, for inverting both velocities and anelastic absorption. Indeed, the estimated Earth macro-model is composed of several homogeneous blocks with average values obtained by the back-propagation of residuals along the ray paths that crossed them.

Another aspect of our method that may require further developments is the possible frequency dependence of the Q factor. Within the frequency range used for normal seismic surveys, e.g., between 10 and 100 Hz, the assumption of a simple linear relationship is acceptable (Ward & Toksöz 1971). The frequency shift method used for the Q macro-model relies on this assumption. It is an open question if this is correct, or not, for ultra-low frequencies, i.e., lower than 1 Hz. Instead, when it comes to the high frequency side, we might split the signal into a few adjacent bands and process each of them separately, so getting a frequency-dependent estimation.

In the macro-models for velocity and Q factor, the layer interfaces are estimated by reflection tomography, inverting picked traveltimes. The only requirement is that these reflections are observable, and this happens when sharp changes occurs for these rock parameters. In most cases these changes are coupled, but not always. Lines *et al.* (2008, 2011) showed that reflections may be caused by variations in the Q factor only, while keeping very similar elastic moduli across an interface. For this reason, velocity and anelastic absorption are estimated separately in our implementation. They are tightly linked, nevertheless, because the ray paths used for the inversion are the same, and also because equation (3) depends on those velocities for converting the anelastic absorption α into the Q factor.

Although the examples presented in this paper are in 2D, the related theory and even the developed software work in both 2D and 3D. The P-velocity macro-model is estimated by the traveltime inversion based on minimum-time ray tracing, which is purely kinematic: so, it does not depend on 2D or 3D propagation properties. The Q-factor macro-model is estimated by the wavelets' spectral centroids, which do not depend on amplitude decays due to 2D or 3D propagation, but only on the frequency-dependent absorption along the ray paths. For the Q-factor micro-model, a 2D or 3D migration algorithm must be chosen according to the data dimensionality.

Application examples with real 3D data to compute P velocity were presented by Vesnaver *et al.* (2000, 2003) and Q factor by Rossi *et al.* (2001, 2007, 2011). The computational cost for the tomographic inversion is quite lower than that one for pre-stack depth migration. However, the 2D implementations may easily run in standard computers in scalar mode, while the 3D runs need parallel coding and hardware.

The source estimation for the Q-factor tomography may be obtained by analysing the Vibroseis sweep on land or the near-field hydrophone at sea; eventually, also some very shallow reflection or direct arrival could be used as viable approximations. Our visco-acoustic estimation is another approximation for the real Earth, which may actually involve complex rheologies, as poro-visco-

elasticity: thus, we may expect interferences of S and converted waves with primaries in the real seismic records. However, the super-position points of the different signals are a few ones only when the channel number is high, and so they are averaged out by the summation process implicit in both tomography and migration. Fortunately, the low amplitude of S waves at small offsets and the relevant move-out difference with respect to P waves minimizes the interpretation ambiguities.

Another practical problem when dealing with real data or complex Earth models is the choice of the time window (and its possible smoothing parameters) for the seismic signal, whose spectrum is used for the Q-factor estimation. Ideally, it should encompass perfectly an entire wavelet only; in practice, we may have some additional interfering event in the same window, or simply its length could be not optimal. Occasional interfering events may be averaged out statistically by tomography and migration, but spatially consistent phenomena, as apparent absorption effects due to thin layers, may degrade our estimates.

The seismic data we modelled is band-limited, so getting a broadband estimation for the Q factor may seem inconsistent. However, in practice, we are injecting additional frequencies by the macro-model parametrization, assuming an Earth composed of layers and blocks with sharp interfaces.

Because of the Gibbs phenomenon, these discontinuities produce ripples that well visible, for example, in the Figure 12. The spectra of the macro-model contain visible frequency peaks beyond 50 Hz, which is an upper limit instead in the high-frequency component. This high-frequency part should be removed from the macro-model spectra because its use relies on an implicit assumption that may be unfitting, i.e., that sharp velocity changes occur at the interfaces between layers.

Indeed, reflections may occur because of density changes only. Instead, the low-frequency contribution due to this model parametrization is more solid, as it is based of physical and geological observations. First, the actual velocities and Q factors of the Earth are positive, and so their average is positive too, which is the zero-frequency component (bias). Second, the natural rock compaction due to the overburden weight produces normally a velocity increase as a function of depth. This

vertical gradient may be reconstructed by a few layers spanning the model up to the target depth. So, the “*a priori*” information built in the macro-model design is what controls the spectral broadening of the estimated model in the low frequency side.

The low- and high-frequency components of the Earth model for the Q factor are computed by quite different procedures. This is not unusual in seismic data processing: for example, the low-frequency component of the acoustic impedance is normally obtained by velocity analysis, while the high-frequency part comes from the reflectivity. Although that hybrid method is not rigorous from the theoretical point of view, it works nicely and has been a standard tool for decades. For the Q factor modelling, the link between low- and high-frequency components obtained by Q tomography and instantaneous frequency is tighter. In the Appendix 2, we prove that the spectrum centroid of a wavelet can be obtained from the time-averaged instantaneous spectrum of a normalized complex trace.

The appropriate procedure for linking micro- and macro model is getting the optimal bands and weights for the anelastic absorption $\alpha(\mathbf{x})$, substituting the resulting broadband estimate into equation (4). One reason is the linearity in the $\alpha(\mathbf{x})$ estimation, which is lost when the Q factor is computed. Another reason is the missing continuous component (or bias) in the micro-model, causing several zero-crossings or tiny values that may turn into major spikes when their inverse is computed. The continuous component obtained by tomography, when added into the broadband estimation, avoids any need for constraints or regularizations.

7 CONCLUSIONS

We introduced a new hybrid method for a broadband imaging of the Q-factor contrast in depth. Our approach for estimating the Q factor is analogous to the idea of combining tomography and migration, proposed for seismic reflectivity by Mora (1989) and by Tura *et al.* (1998) for AVO

attributes. It resembles also a classic, popular approach for estimating the acoustic impedance from seismic traces (Lavergne 1975; Lindseth 1976; Lavergne and Willm 1977; Becquey *et al.* 1979), where the low-frequency trend is provided by stacking velocities, while the high-frequency component comes from the deconvolved traces. Our method is not a full-waveform inversion in a strict sense, as it analyses a few sparse waveforms only for the low-frequency component, and relies on the instantaneous frequency migration for the high-frequency information. However, we believe that it may provide a broadband initial model for more rigorous inversion procedures. Tomographic inversion of picked events provides mainly the low spatial frequencies, whilst the higher ones come from the depth imaging of the instantaneous frequency.

As migration is collapsing diffractions into the corresponding structural features, we may expect such a signal enhancement not only for the reflectivity, but also for the instantaneous frequency. Both migration and tomography decrease the contribution of random scattering and diffractions to the total observed absorption, so reducing the gap between estimated and intrinsic absorption, due to filling fluids and anelastic phenomena. In addition, migration is a powerful filter for reducing the noise, by strengthening signals that propagate according to the wave equation in a given velocity field. On the other hand, migration is sensitive to major spikes in the data. This would be a major drawback when adopting conventional algorithms for the instantaneous frequency calculation, where spikes show up where phase unwrapping algorithms fail. Instead, a smooth estimate is obtained when using the algorithm proposed by Poggiagliolmi & Vesnaver (2014), which does not require any user-defined parameter.

The presented Q-factor broadband imaging is a hybrid method that does not belong to the full-waveform inversion family, but allows building a better initial Earth model for more accurate estimations of rock velocity and anelastic absorption by those methods. This is a critical aspect, because the cross-talk between velocity and Q factor during their joint inversion causes significant ambiguities (Mulder & Hak 2009 a, b). Quantifying such a benefit, however, requires further studies.

ACKNOWLEDGEMENTS

Our work was supported by the grants n. FIR15001 and FIR15002 from the Petroleum Institute Research Centre (Abu Dhabi, United Arab Emirates), currently part of the Khalifa University of Science and Technology. We thank Davide Gei and Umberta Tinivella (OGS, Italy) for their assistance in using various computing codes. We thank John Stockwell for the Seismic Un*x software (Stockwell 1997, 1999; Cohen & Stockwell, 2013), which we used for the pre-stack depth migration of seismic data, and Sergey Pavlukhin for the SeiSee software (Pavlukhin, 2013), which we used for most plots. Finally, we thank Claudio Bagaini and Jean Virieux for several constructive remarks.

REFERENCES

- Ackroyd, M. H., 1970. Instantaneous spectra and instantaneous frequency. *Proceedings IEEE*, **58**, 141.
- Amoroso, O., Russo, G., De Landro, G., Zollo, A., Garambois, S., Mazzoli, S., Parente, M. & Virieux, J., 2017. From velocity and attenuation tomography to rock physical modelling: Inferences on fluid-driven earthquake processes at the Irpinia fault system in Southern Italy. *Geophysical Research Letters*, **44**, 6752-6760.
- Becquey, M., Lavergne, M. & Willm, C., 1979. Acoustic impedance log computed from seismic traces. *Geophysics*, **44**, 1485-1501.
- Billette, F. & Lambaré, G., 1998. Velocity macro-model estimation by stereotomography. *Geophysical Journal International*, **135**, 671-680.

- Billette, F., Le Begat, S., Podvin, P. & Lambaré, G., 2003. Practical aspects and applications of 2D stereotomography. *Geophysics*, **68**, 1008-1021.
- Carcione, J. M., 1992. Modelling anelastic singular surface waves in the Earth. *Geophysics*, **57**, 781-792.
- Carcione, J. M., 2014. *Wave Fields in Real Media. Theory and numerical simulation of wave propagation in anisotropic, anelastic, porous and electromagnetic data – (third edition)*. Elsevier, 690 pp.
- Casula, G. & Carcione, J. M., 1992. Generalized mechanical model analogies of linear viscoelastic behaviour. *Bollettino di Geofisica Teorica ed Applicata*, **34**, 235-256.
- Cohen, J. K. & Stockwell, Jr. J. W., 2013. CWP/SU: Seismic Un*x release 43R5, an open source software package for seismic research and processing, Centre for Wave Phenomena, Colorado School of Mines, <http://timna.mines.edu/cwpcodes/>.
- Cheng, P. & Margrave, G. F., 2012. Q estimation by a match-filter method. Expanded Abstract, SEG Annual Meeting, 1-5.
- Dasgupta, R. & Clark, R. A., 1998. Estimation of Q from surface seismic reflection data. *Geophysics*, **63**, 2120-2128.
- Dupuy, B., Garambois, S. & Virieux, J., 2016a. Estimation of rock physics properties from seismic attributes – Part 1: Strategy and sensitivity analysis. *Geophysics*, **81**, M35-M53.
- Dupuy, B., Garambois, S., Asnaashari, A., Balhareth, H. M., Landrø, M., Stovas, A. & Virieux, J., 2016b. Estimation of rock physics properties from seismic attributes – Part 2: Applications. *Geophysics*, **81**, M55-M69.
- Fei, W. & McMechan, G. A., 2006. CRP-based seismic migration velocity analysis. *Geophysics*, **71**, U21-U28.

- Futterman, W. I., 1962. Dispersive body waves. *Journal of Geophysical Research*, **67**, 5279-5291.
- Guillaume, P., Audebert, F., Berthet, P., David, B., Herrenschmidt, A. & Zhang, X., 2001. 3D finite-offset tomographic inversion of CRP-scan data, with or without anisotropy. Expanded Abstracts, SEG Annual Meeting, 718-721.
- Hak, B. & Mulder, W. A., 2011. Seismic attenuation imaging with causality. *Geophysical Journal International*, **184**, 439-451.
- Hackert, C. L. & Parra, J. O., 2003. Estimating scattering attenuation from vugs and karst. *Geophysics*, **68**, 1182-1188.
- Hackert, C. L. & Parra, J. O., 2004. Improving estimates from seismic reflection data using well-log-based localized spectral correction. *Geophysics*, **69**, 1521-1529.
- Hubral, P. & Krey, Th., 1980. Interval velocities from seismic reflection travelttime measurements. SEG, Tulsa.
- Jannsen, D., Voss, J. & Theilen, F., 1985. Comparison of methods to determine Q in shallow sediments from vertical reflection seismograms. *Geophysical Prospecting*, **33**, 479-497.
- Kjartansson, E., 1979. Constant Q-wave propagation and attenuation. *Journal of Geophysical Research*, **84**, 4137-4748.
- Kosloff, R. & Kosloff, D., 1986. Absorbing boundaries for wave propagation problems. *Journal of Computational Physics*, **63**, 363-376.
- Lavergne, M., 1975. Pseudo diagraphies de vitesse en offshore profond. *Geophysical Prospecting*, **23**, 695-711.
- Lavergne, M., and Willm, C., 1977. Inversion of seismograms and pseudo-velocity logs. *Geophysical Prospecting*, **25**, 232-250.

- Larner, K., Hatton, L., Gibson, B. & I-Chi, Hsu, 1981. Depth migration of imaged time sections. *Geophysics*, **46**, 734-750.
- Lindseth, R. O., 1976. Seislog process uses seismic reflection traces. *Oil and Gas Journal*, **38**, 481-488.
- Lines, L. R., Vasheghani, F., Treitel, S. & Ulrych, T., 2008. Reflections on Q. *CSEG Recorder*, December, 36-38.
- Lines, L. R., Sondergeld, C., Innanen, K., Wong, J., Treitel, S. & Ulrych, T., 2011. Experimental confirmation of "Reflections on Q". CREWES Research Report, **23**, 1-7.
- Mazzotti, A., 1991. Amplitude, phase and frequency versus offset applications. *Geophysical Prospecting*, **39**, 863-886.
- Mora, P. R., 1989. Inversion = migration + tomography. *Geophysics*, **54**, 1575-1586.
- Mulder, W. A. & Hak, B., 2009a. An ambiguity in attenuation scattering imaging. *Geophysical Journal International*, **178**, 1614-1624.
- Mulder, W. A. & Hak, B., 2009b. Velocity and attenuation perturbation can hardly be determined simultaneously in acoustic attenuation scattering. Expanded Abstracts, SEG Annual Meeting, 3078-3082.
- Nur, A., 1989. Four-dimensional seismology and (true) direct detection of hydrocarbons: the petrophysical basis. *The Leading Edge*, **8**, 30-36.
- Operto, S., Ravaut, C., Improta, L., Virieux, J. & Dell'Aversana, P., 2004. Quantitative imaging of complex structures from dense wide-aperture seismic data by multiscale travelttime and waveform inversion: a case study. *Geophysical Prospecting*, **72**, 625-651.
- Pavlukhin, S., 2013. SeiSee software, Version 2.22.2. Dalmorneftegeofizika Geophysical Company, Russia, <http://www.dmng.ru/seisview>.

- Plessix, R. E., 2008. Introduction: Towards a full waveform inversion. *Geophysical Prospecting*, **56**, 761-763.
- Poggiagliolmi, E. & Vesnaver, A., 2014. Instantaneous phase and frequency derived without user-defined parameters. *Geophysical Journal International*, **199**, 1544-1533.
- Poggiagliolmi, E., Accaino, F. & Vesnaver, A., 2016. The broadband response of a displacement sensor. Expanded Abstracts, SEG Annual Meeting, 147-151.
- Quan, Y. & Harris, J., 1997. Seismic attenuation tomography using the frequency shift method. *Geophysics*, **62**, 895-905.
- Raikes, S. A. & White, R. E., 1984. Measurements of Earth attenuation from downhole and surface seismic recordings. *Geophysical Prospecting*, **32**, 892-919.
- Ribodetti, A. & Virieux, J. 1998. Asymptotic theory for imaging the attenuation factor Q. *Geophysics*, **63**, 1767-1778.
- Rossi, G., Madrussani, G. & Vesnaver, A., 2000. Adaptive 3D joint inversion of direct, reflected and refracted arrivals. In: *Experimental Acoustic Inversion Methods for Exploration of the Shallow Water Environment* (eds. Caiti, A., Hermand, J.-P., Jesus, S.M. & Porter, M.B.), 235-248. Dordrecht, Kluwer.
- Rossi, G., Corubolo, P., Böhm, G., Ceraggioli, E., Dell'Aversana, P., Morandi, S., Poletto, F. & Vesnaver, A., 2001. Joint 3D inversion of SWD and surface seismic data. *First Break*, **19**, 453-459.
- Rossi, G. & Vesnaver, A., 2001. Joint 3D travelttime inversion of P, S and converted waves. *Journal of Computational Acoustics*, **9**, 1407-1416.
- Rossi, G., Gei, D., Böhm, G., Madrussani, G. & Carcione, J. 2007. Attenuation tomography: an application to gas-hydrate and free-gas detection. *Geophysical Prospecting*, **55**, 655-669.

- Rossi, G., Chadwick, R. A. & Williams, G. A. 2011. Traveltime and attenuation tomography of CO₂ plume at Sleipner. Expanded Abstracts, EAGE Annual Meeting, A039.
- Saha, J. G., 1987. Relationship between Fourier and instantaneous frequency. Expanded Abstracts, SEG Annual Meeting, 591-594.
- Spencer, T. W., Sonnad, J. R. & Butler, T. M. 1982. Seismic Q-stratigraphy or dissipation. *Geophysics*, **47**, 16-24.
- Stockwell, Jr. J. W., 1997. Free Software in Education: A case study of CWP/SU: Seismic Un*x. *The Leading Edge*, **16**, 1045-1049.
- Stockwell, Jr. J. W., 1999. The CWP/SU: Seismic Un*x package. *Computers & Geosciences*, **25**, 415-419.
- Sword, C., 1986. Tomographic determination of interval velocities from picked reflection seismic data. Expanded Abstracts, SEG Annual Meeting, 657-660.
- Taner, M.T., Koehler, F. & Sheriff, R. E., 1979. Complex seismic trace analysis. *Geophysics*, **44**, 1041-1063.
- Taner, M.T. & Koehler, F., 1981. Surface consistent corrections. *Geophysics*, **46**, 17-22.
- Tarantola, A., 1984. Inversion of seismic reflection data in the acoustic approximation. *Geophysics*, **49**, 1259-1266.
- Tonn, R., 1991. The determination of seismic quality factor Q from VSP data: a comparison of different computational methods. *Geophysical Prospecting*, **39**, 1-27.
- Tura, A., Hanitzsch, C. & Calandra, H., 1998. 3-D AVO migration/inversion of field data. *The Leading Edge*, **17**, 1578-1578.

- van der Sluis, A. & van der Vorst, H. A., 1987. Numerical solutions of large, sparse linear algebraic systems arising from tomographic problems. In: Nolet G. (ed.), *Seismic Tomography with Applications in Global Seismology and Exploration Geophysics*. D. Reidel Publishing Company, Dordrecht, the Netherlands.
- Vesnaver, A., 1996. Ray tracing based on Fermat's principle in irregular grids. *Geophysical Prospecting*, **44**, 741-760.
- Vesnaver, A., Böhm, G., Madrussani, G., Petersen S. & Rossi, G., 1999. Tomographic imaging by reflected and refracted arrivals at the North Sea. *Geophysics* **64**, 1852-1862, doi:10.1190/1.1444691.
- Vesnaver, A. & Böhm, G., 2000. Staggered or adapted grids for seismic tomography? *The Leading Edge*, **19**, 944-950.
- Vesnaver, A., Böhm, G., Madrussani, G., Rossi, G. & Granser, H., 2000. Depth imaging and velocity calibration by 3D adaptive tomography. *First Break*, **18**, 303-312.
- Vesnaver, A., Accaino, F., Böhm, G., Madrussani, G., Pajchel, J., Rossi, G. & Dal Moro, G., 2003. Time-lapse tomography. *Geophysics*, **68**, 815-823.
- Vesnaver, A., 2017. Instantaneous frequency and phase without unwrapping. *Geophysics*, **82**, F1-F7.
- Ville, J., 1948. Theorie et applications de la notion de signal analytique. *Cables et Transmission*, **2**, 61-74.
- Ward, R. W. & Toksöz, M. N., 1971. Causes of regional variation of magnitude. *Bulletin of the Seismological Society of America*, **61**, 649-670.
- White, J. E., 1966. Static friction as a source of seismic attenuation. *Geophysics*, **31**, 333-339.

Wu, R., 1985. Multiple scattering and energy transfer of seismic waves — separation of scattering effect from intrinsic attenuation — I. Theoretical modelling. *Geophysical Journal International*, **82**, 57-80.

Yilmaz, Ö., 2001. Seismic data analysis. SEG, Tulsa, 2065 pp.

Zucca, J. J., Hutchings, L. J. & Kasameyer, P. W., 1994. Seismic velocity and attenuation structure of the Geysers geothermal field, California. *Geothermics*, **23**, 111-126.

Appendix 1 Linear combination coefficients

We get an optimal linear combination of the high- and low-frequency components to match a broad-band model by minimizing the energy of their difference **D**:

$$\mathbf{D} = (\lambda_1 \mathbf{L} + \lambda_2 \mathbf{H} - \mathbf{B}) \quad , \quad (\text{A1-1})$$

where **L** and **H** are vector or matrices with the estimated low- and high-frequency components of the model, respectively. **B** is either the actual Earth model – (known in simulations, for example) – or a set of well logs, in a real case. In two dimensions, **D** is a matrix. We define a quadratic object function *Q* as follows:

$$Q = \frac{1}{2} \sum_{ij} d_{ij}^2 = \frac{1}{2} \sum_{ij} (\lambda_1 l_{ij} + \lambda_2 h_{ij} - b_{ij})^2 \quad , \quad (\text{A1-2})$$

where the terms with a double index are the corresponding matrix elements, while λ_1 and λ_2 are the coefficients for the optimal linear combination that we are computing. We get two equations by zeroing the derivatives of *F* with respect to λ_1 and λ_2 :

$$\frac{\partial F}{\partial \lambda_1} = \frac{\partial F}{\partial \lambda_2} = 0 \quad , \quad (\text{A1-3})$$

that is:

$$0 = \sum_{ij} (\lambda_1 l_{ij} + \lambda_2 h_{ij} - b_{ij}) l_{ij} \quad , \quad (\text{A1-4})$$

$$0 = \sum_{ij} (\lambda_1 l_{ij} + \lambda_2 h_{ij} - b_{ij}) h_{ij} \quad .$$

Rearranging and using a more compact notation as:

$$\sum_{ij} x_{ij} y_{ij} \equiv \underline{xy} \quad \text{and} \quad \sum_{ij} x_{ij} x_{ij} \equiv \underline{x^2} \quad , \quad (\text{A1-5})$$

we may the equation system (A1-4) as:

$$\lambda_1 \underline{l^2} + \lambda_2 \underline{lh} = \underline{lb} \quad , \quad (\text{A1-6})$$

$$\lambda_1 \underline{lh} + \lambda_2 \underline{h^2} = \underline{hb} \quad .$$

This system has solutions only if its determinant Det does not vanish, i.e.:

$$Det = \underline{l^2 h^2} - (\underline{lh})^2 \neq 0 \quad . \quad (A1-7)$$

In that case, the solutions for λ_1 and λ_2 are:

$$\lambda_1 = \frac{1}{Det} (\underline{lb h^2} - \underline{lh hb}) \quad , \quad (A1-8)$$

$$\lambda_2 = \frac{1}{Det} (\underline{hb l^2} - \underline{lh lb}) \quad .$$

Appendix 2 Ackroyd's theorem review

Ackroyd (1970) stated an important theorem linking the instantaneous frequency with the centroid of the instantaneous spectrum of an analytic signal, better known as a complex trace by geophysicists. Here we review shortly its validity range and the link between the instantaneous frequency with the wavelet spectra centroids used by the method of Quan & Harris (1997) to estimate the anelastic absorption.

Adopting Ackroyd's notation, let us indicate by $m(t)$ an analytic function of time t and by $M(f)$ its Fourier transform, which depends on frequency f . The instantaneous spectrum $e(t, f)$, also called time-frequency energy density distribution by Ville (1948), is defined as:

$$e(t, f) = m(t) M^*(f) \exp(-2 \pi i f t) \quad , \quad (A2-1)$$

where $*$ indicates complex conjugation and i is the imaginary unit. The centroid $f_c(t)$ (or normalized first moment) of the real part of $e(t, f)$ with respect to frequency f is:

$$f_C(t) = \text{Re} \left[\int_{-\infty}^{\infty} f e(t, f) df / \int_{-\infty}^{\infty} e(t, f) df \right] \quad . \quad (\text{A2-2})$$

By substituting (A2-1) into (A2-2), we get:

$$f_C(t) = \frac{1}{2\pi i} \text{Re} [\dot{m}^*(t) / m^*(t)] \quad , \quad (\text{A2-3})$$

where $\dot{m}(t)$ indicates a time derivative. At this point, the next step of Ackroyd's derivation needs an assumption that is implicit in his paper, but it must be declared instead. If the function $m(t)$ is very general, it may be expressed in polar form as:

$$m(t) = A(t) \exp(i \phi(t)) \quad , \quad (\text{A2-4})$$

where $A(t)$ is the envelope and $\phi(t)$ is the instantaneous phase. The time derivative $\dot{m}(t)$ is then:

$$\dot{m}(t) = \dot{A}(t) \exp(i \phi(t)) + A(t) i \exp(i \phi(t)) \dot{\phi}(t) = \dot{A}(t) \exp(i \phi(t)) + i m(t) \dot{\phi}(t) \quad . (\text{A2-5})$$

Only if we assume that:

$$\dot{A}(t) \approx 0 \quad , \quad (\text{A2-6})$$

i.e., if the envelope is constant or very smooth, we get the final Ackroyd's formula by using (A2-5)

and (A2-6) in (A2-3):

$$f_C(t) = \frac{1}{2\pi} \dot{\phi}(t) \quad , \quad (\text{A2-7})$$

which relates the instantaneous frequency $\dot{\phi}(t)$ to the centroid $f_C(t)$ of the instantaneous spectrum. We remark that the assumption (A2-6) is exact only at the envelope maxima or minima, as pointed out also by Saha (1987) and Mazzotti (1991). However, in the special case of a normalized

complex trace, obtained by dividing the trace by its envelope, the approximation (A2-6) becomes an exact relation, and so it makes (A2-7) an exact relation too.

In the special case of a normalized complex trace, i.e., $m(t) = \exp(i \phi(t))$, the denominator term in equation (A2-2) simplifies:

$$\int_{-\infty}^{\infty} e(t, f) df = \exp(i \phi(t)) \int_{-\infty}^{\infty} M^*(f) \exp(-2\pi i f t) df =$$

$$= \exp(i \phi(t)) \left[\int_{-\infty}^{\infty} M(f) \exp(2\pi i f t) df \right]^* = \exp(i \phi(t)) [\exp(i \phi(t))]^* = 1. \quad (\text{A2-8})$$

So, in this special case, the denominator is unity and we obtain:

$$f_c(t) = \text{Re} \left[\int_{-\infty}^{\infty} f e(t, f) df \right] = \frac{1}{2\pi} \dot{\phi}(t) \quad . \quad (\text{A2-9})$$

Let us indicate by $\langle \cdot \rangle$ an average over a time window with the duration of a wavelet. Applying this linear operator to (A2-9), we get:

$$\langle f_c(t) \rangle = \text{Re} \left[\int_{-\infty}^{\infty} f \langle e(t, f) \rangle df \right] = \frac{1}{2\pi} \langle \dot{\phi}(t) \rangle \quad . \quad (\text{A2-10})$$

A local average of the instantaneous frequency corresponds to a local average of the instantaneous spectrum and its centroid. Thus, the method of Quan & Harris (1997), which computes the centroid spectrum of time-windowed wavelets, is consistent with our procedure based on the instantaneous frequency of a normalized complex trace. However, its direct applicability to real cases is

questionable, as it makes sense only if the instantaneous frequency $\dot{\phi}(t)$ includes frequency components up to zero: unfortunately, they cannot be provided by standard sensors as geophones and accelerometers, as pointed out by Poggiagliolmi *et al.* (2016).

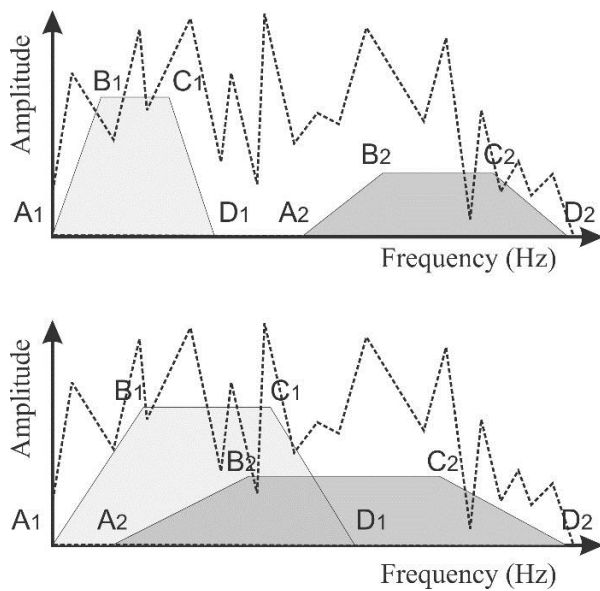


Figure 1. The spectrum of a seismic record (dashed line) may be recorded by two systems with the different amplitude level and different frequency bands, either disjoint (top) or partially overlapping (bottom).

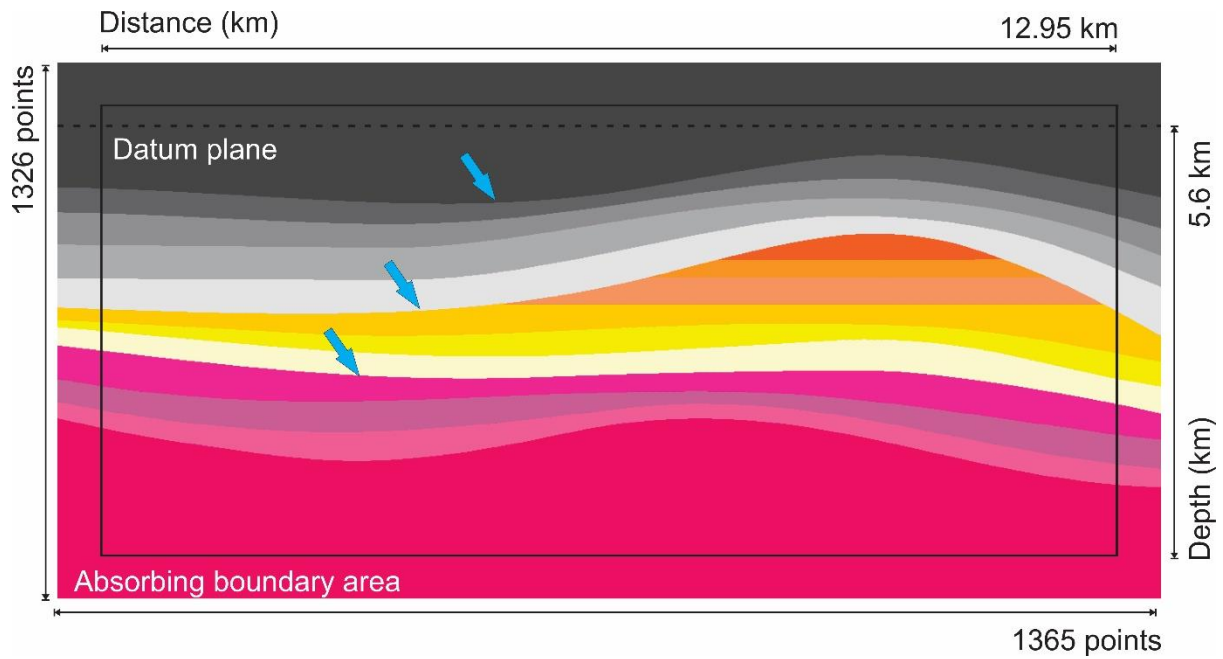


Figure 2. Earth model composed of homogeneous layers with gently bent interfaces with 15 layers. The model is extended outside the black rectangular part to include absorbing boundary conditions for the seismic modelling. The dashed line indicates the datum plane, where sources and receivers are located. The blue arrows indicate the three main horizons used for the tomographic inversion to estimate a macro-model.

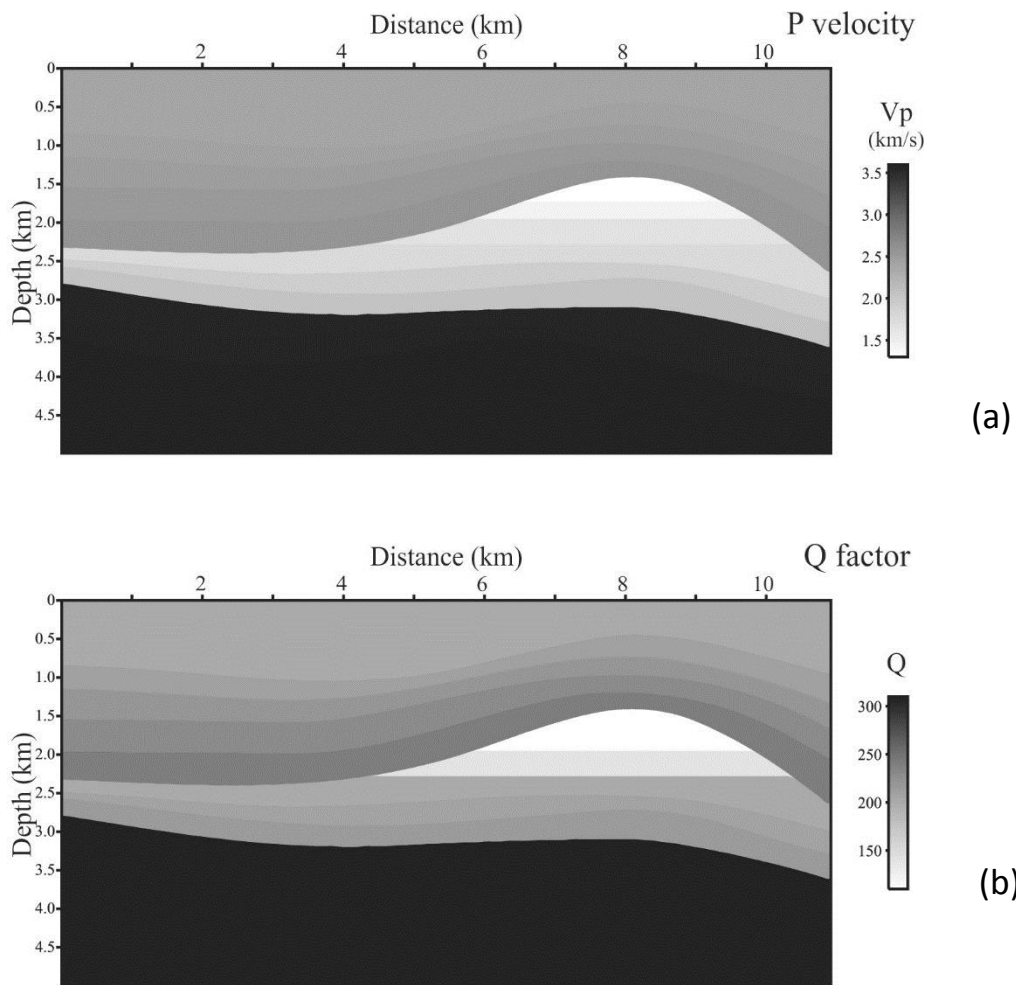


Figure 3. P velocity (a) and Q factor (b) of the model of Figure 2, without any filtering.

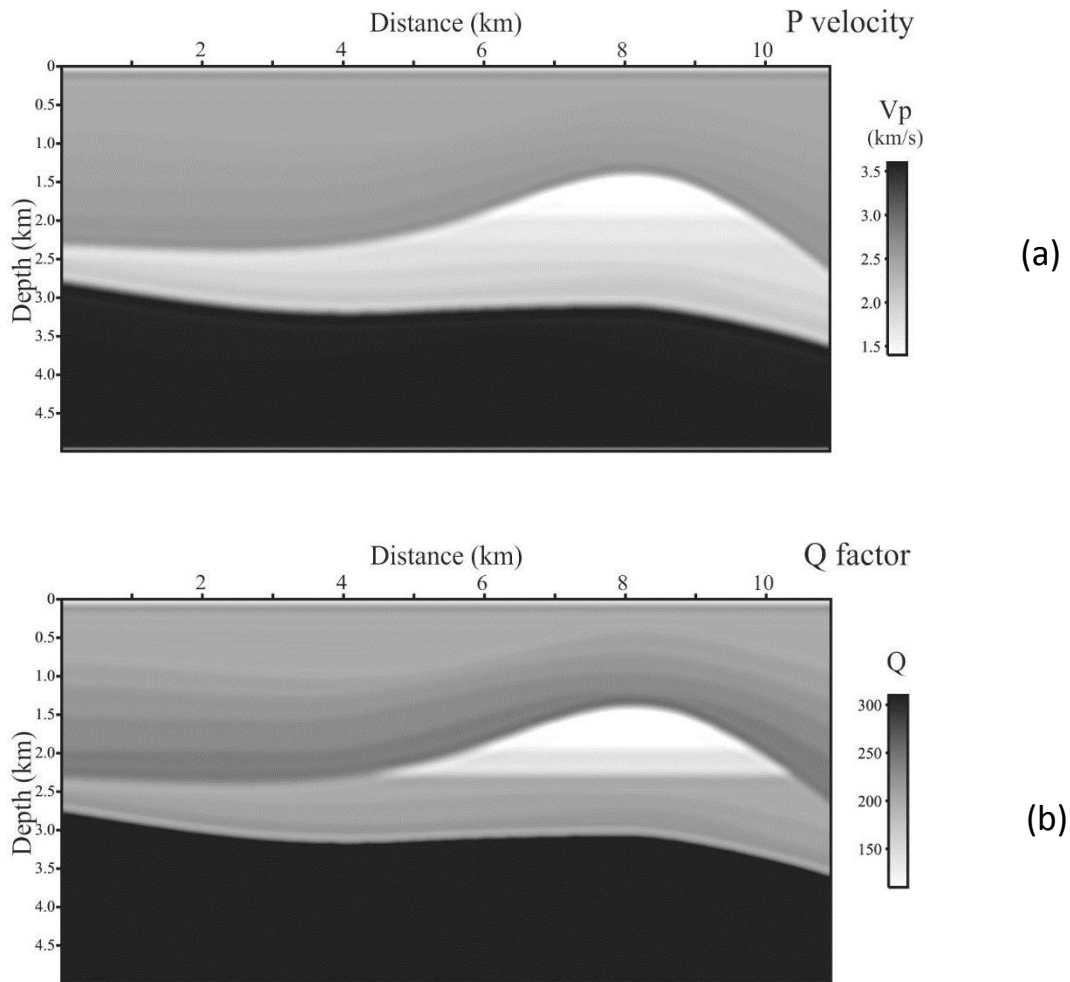


Figure 4. P velocity (a) and Q factor models (b) as in Figure 3 after a low-pass filtering.

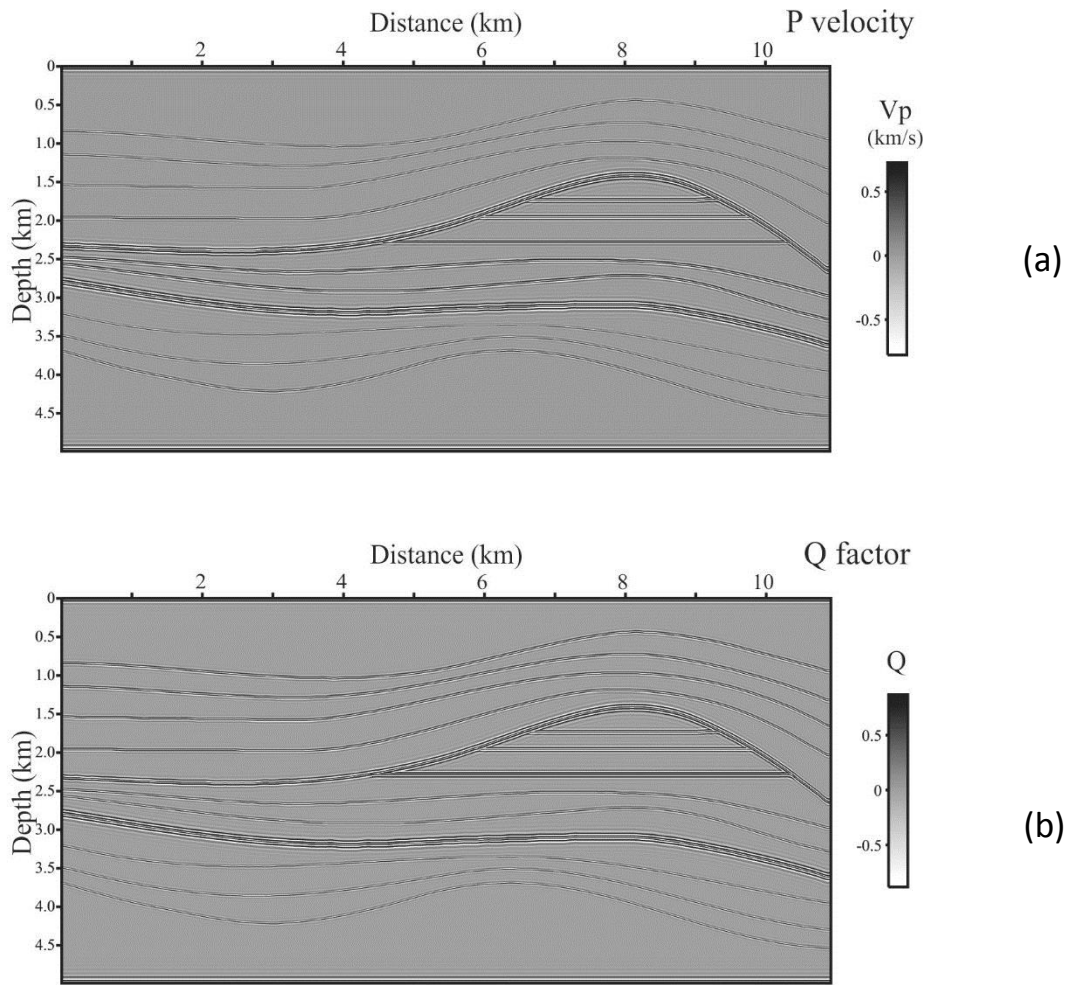


Figure 5. P velocity (a) and Q factor models (b) as in Figure 3 after a high-pass filtering.

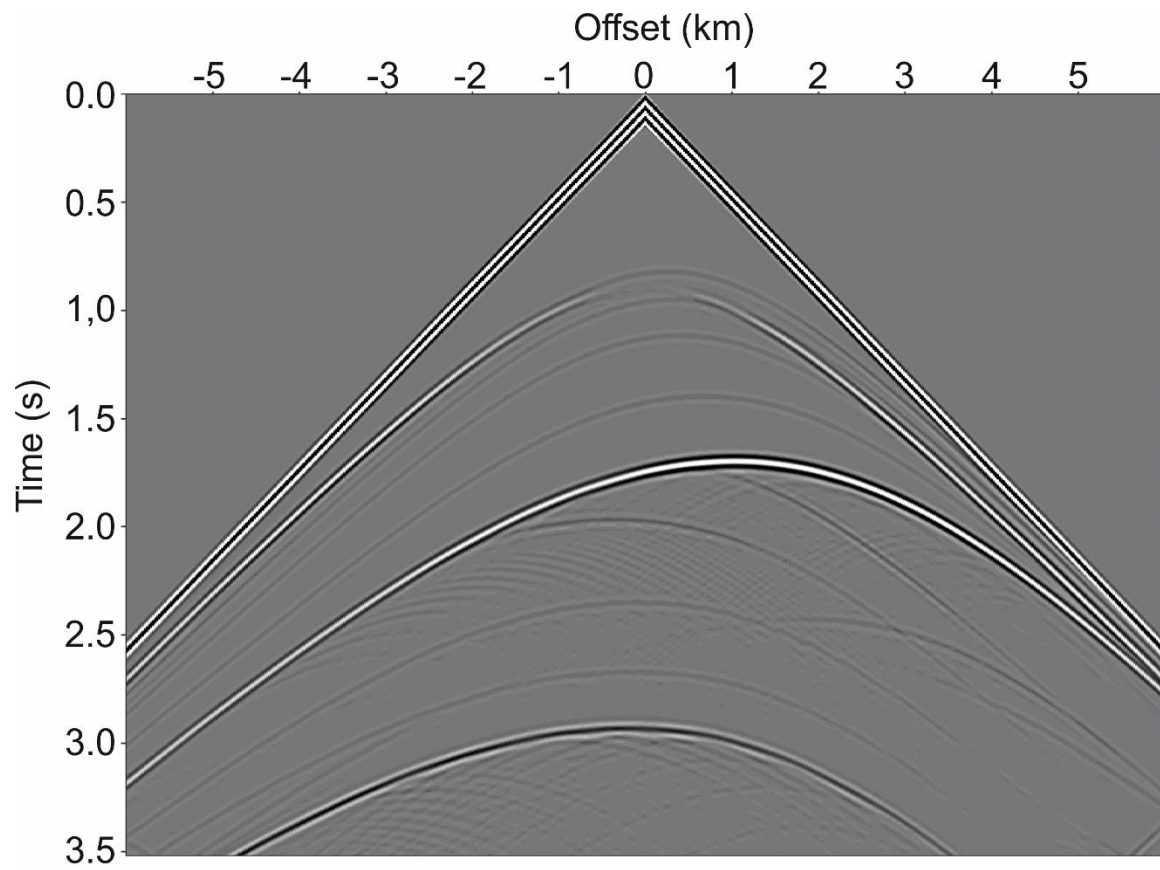


Figure 6. A shot gather at a central shot point of the synthetic survey.

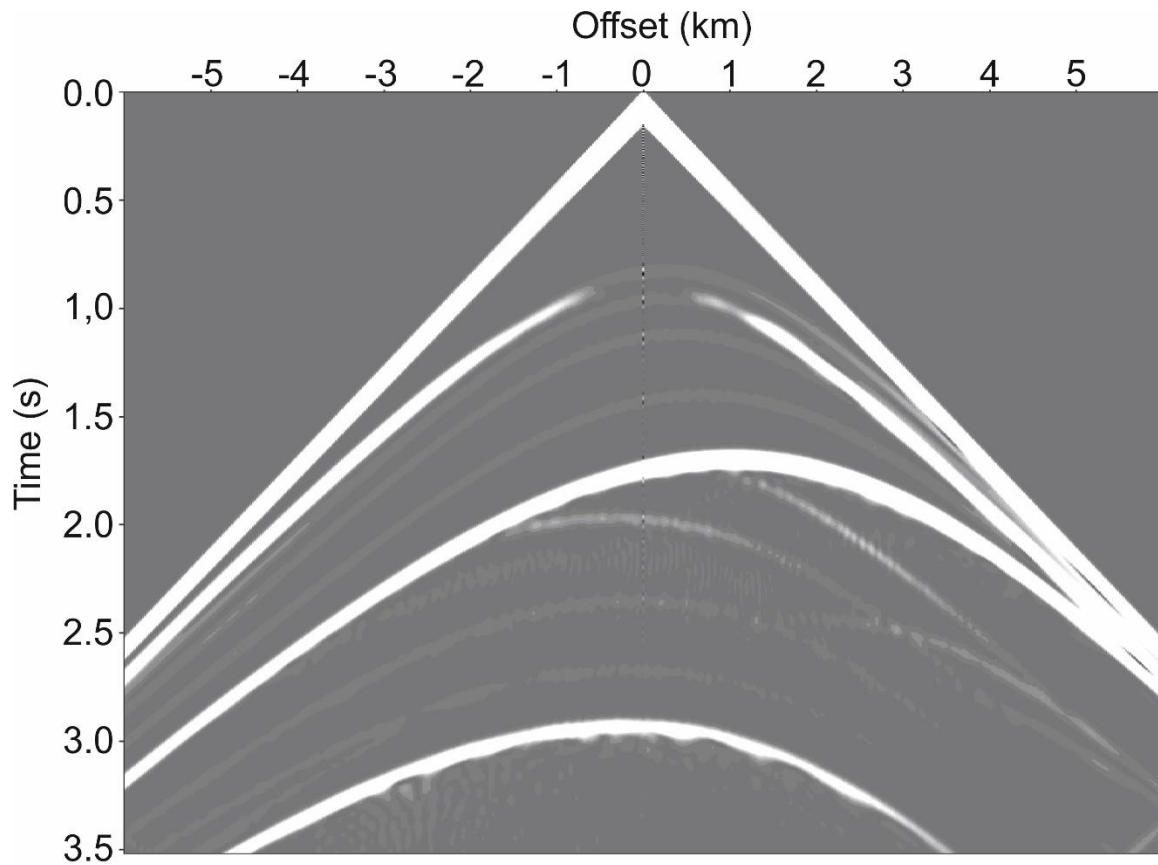


Figure 7. Corresponding instantaneous frequency of the seismic data in Figure 6.

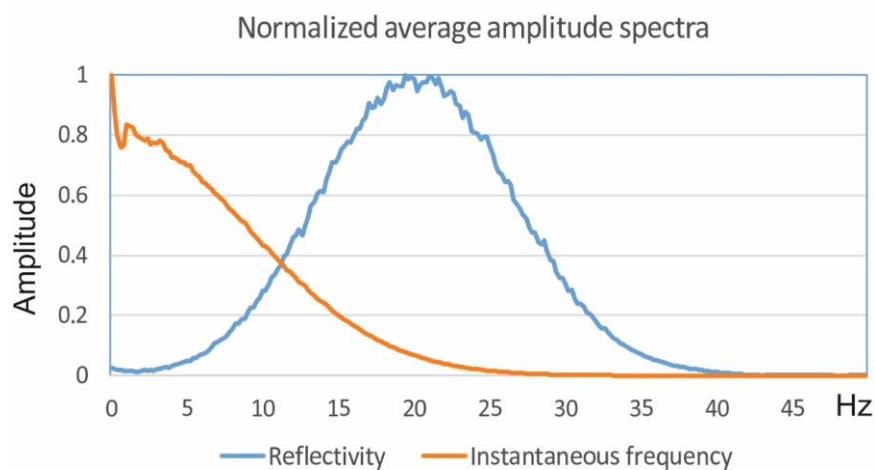


Figure 8. Average amplitude spectra for the shot gathers in Figure 6 (blue line) and its instantaneous frequency in Figure 7 (orange line).

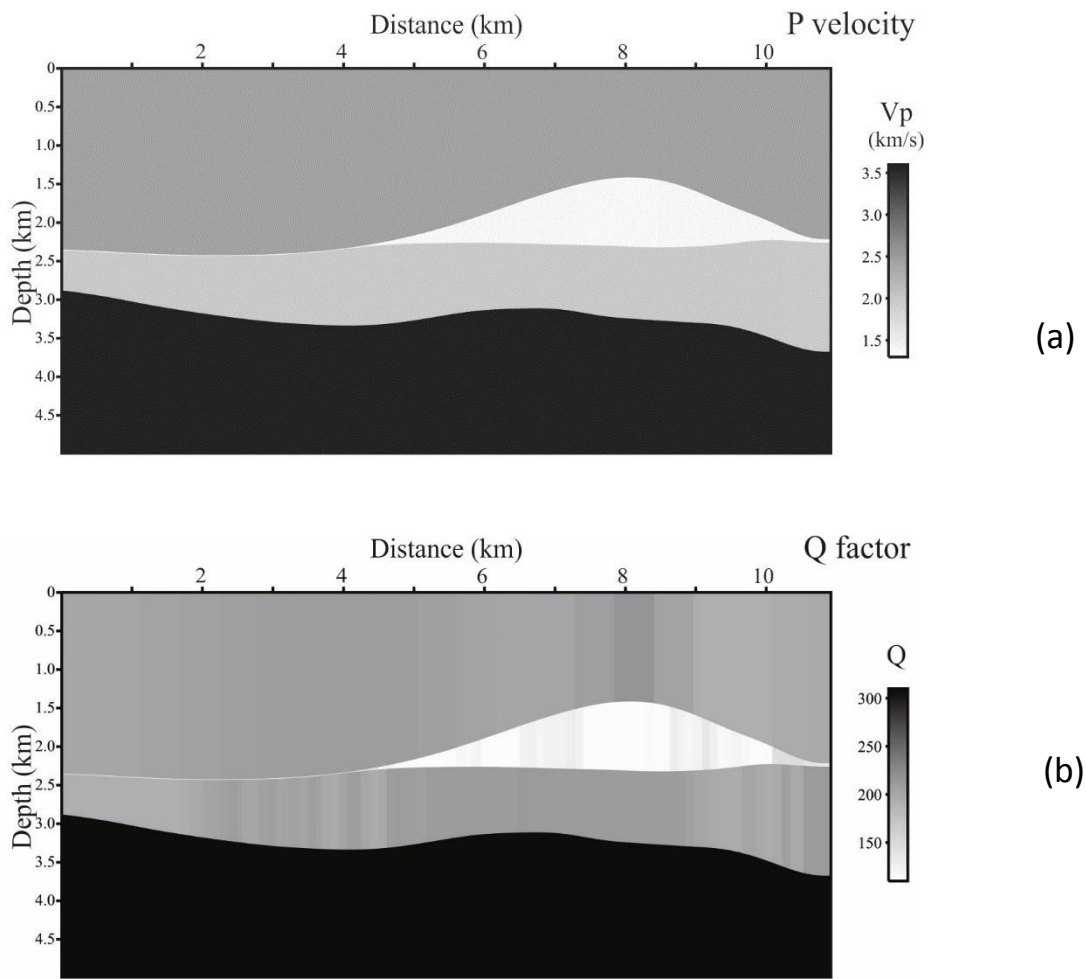
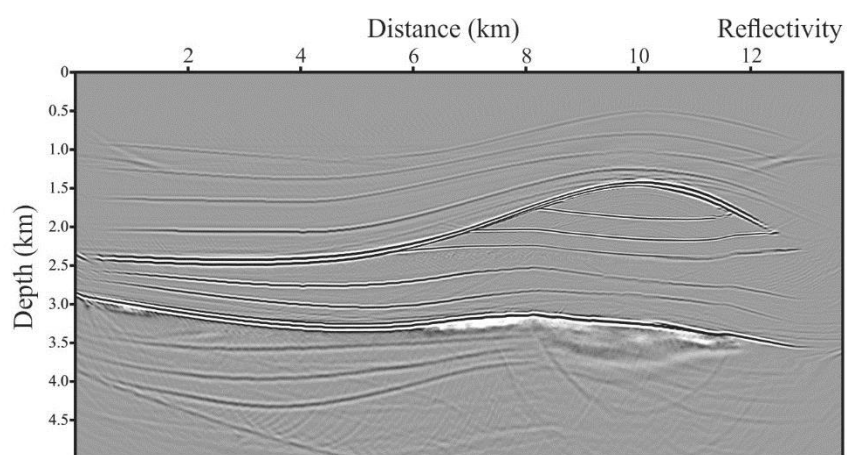
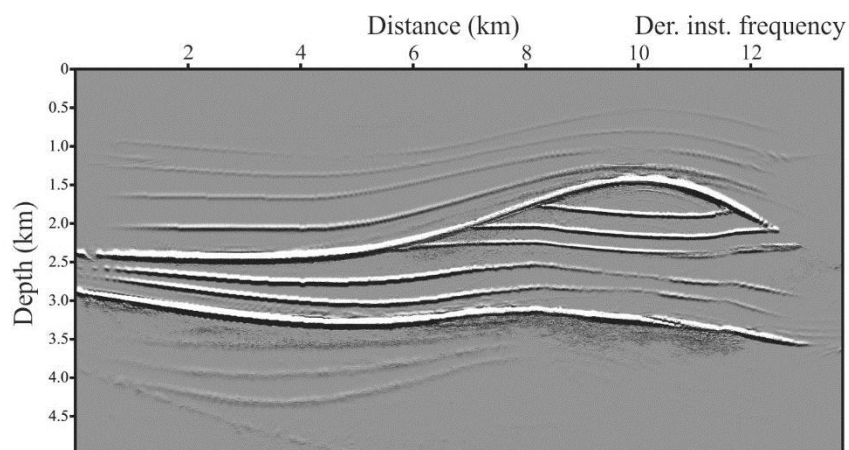


Figure 9. Macro-models obtained from seismic tomography for P velocity (a) and Q factor (b), adopting a staggered grids approach.

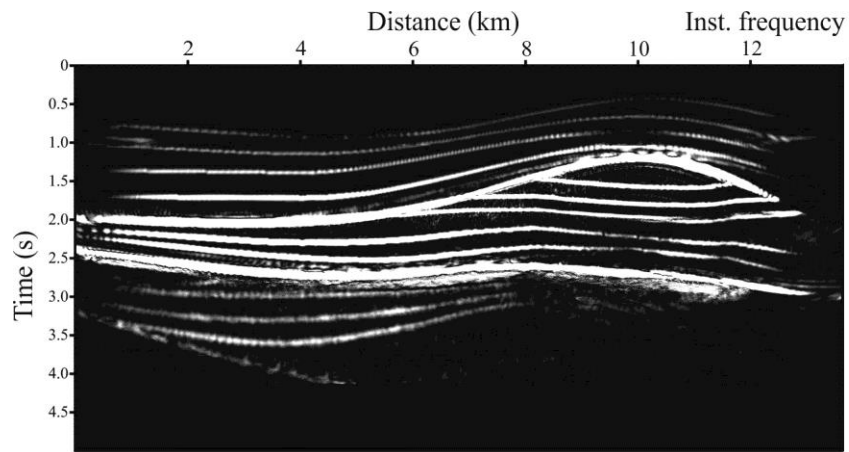


(a)

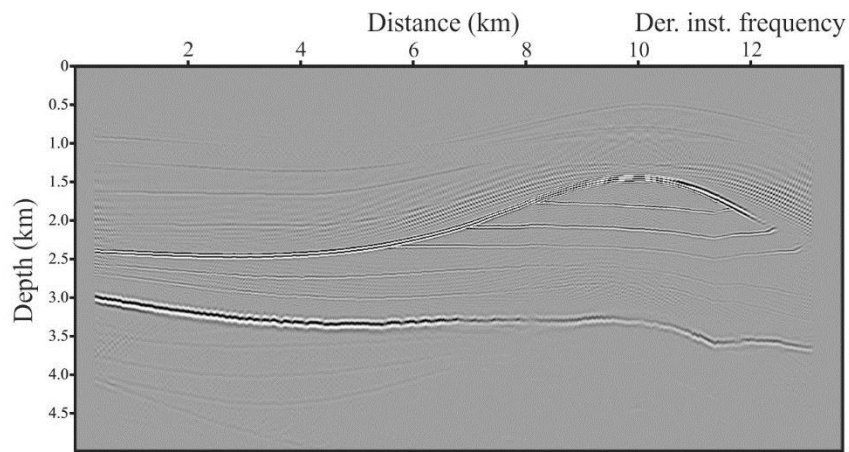


(b)

Figure 10. Pre-stack depth migration of the seismic traces (a) and the corresponding depth migrated and z-derived instantaneous frequency (b), using the P velocity model in Figure 9.



(a)



(b)

Figure 11. Instantaneous frequency of the pre-stack time migrated seismic traces (a) and the corresponding depth converted and z-derived section (b), using the same P velocity model as in Figure 9 and 10.

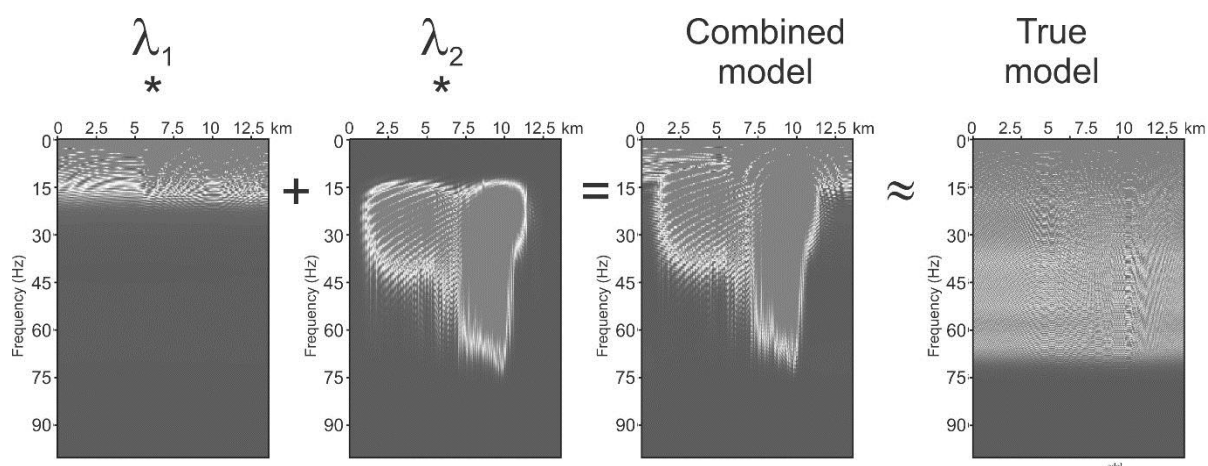


Figure 12. Linear combination of the amplitude spectra of the anelastic absorption coefficient $\alpha(\mathbf{x})$ along the model. From left to right: estimated and filtered macro- and micro-model, broadband combination and true model.

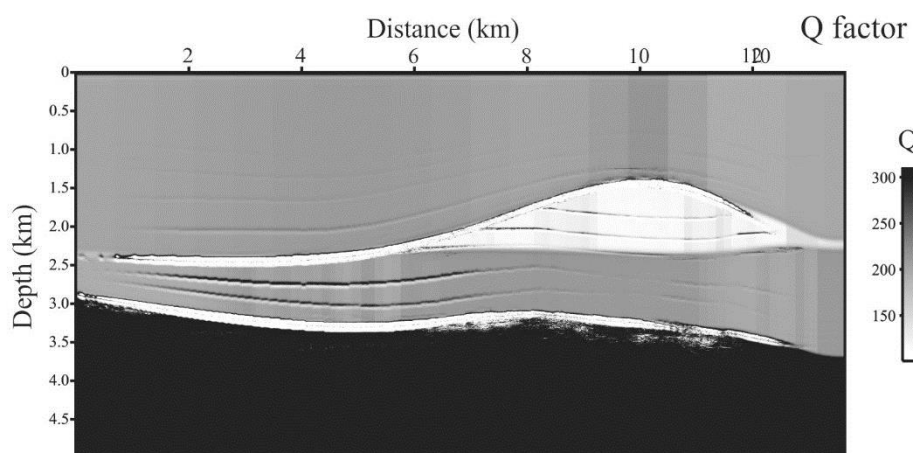


Figure 13. Linear combination of the micro- and macro-model estimated for the Q factor of the detailed Earth model.

Table 1. Visco-acoustic rock parameters for the model in Figure 2, i.e., P velocity, density and Q factor.

Model	Rock parameters			
Layer	V_p (m/s)	ρ (g/cm ³)	Q_p	Color
1	2400	2.3	200	Black
2	2440	2.34	210	Dark Grey
3	2480	2.38	220	Medium Grey
4	2520	2.43	230	Light Grey
5	2580	2.48	240	Very Light Grey
6	1120	1.5	85	Orange
7	1420	1.6	110	Light Orange
8	1660	1.93	140	Light Yellow
9	1780	2.09	200	Yellow
10	1920	2.14	208	Light Yellow
11	2040	2.19	215	Very Light Yellow
12	3549	3.0	415	Pink

13	3575	3.08	420	
14	3613	3.15	425	
15	3670	3.22	430	

Table 2. Comparison of estimated versus true average depths, P velocities and Q factors in the macro-model obtained by reflection tomography.

Layer Number	True Model			Inverted Model			Relative Error	
	True depth average (km)	True V_p average (km/s)	True Q_p factor average	Inverted depth average (km)	Inverted V_p average (km/s)	Inverted Q factor average	V_p	Q_p factor
1	0.50	3.08	77	0.53	3.02	76	2.1%	1%
2	1.06	3.86	115	1.10	3.92	109	1.6%	5%
3	1.61	4.48	175	1.64	4.60	171	2.7%	2%
4	2.00	5.00	250	2.00	5.00	250	0.00%	0%